

COMPUTATIONAL DESIGN OF CREEP-RESISTANT ALLOYS AND EXPERIMENTAL VALIDATION IN FERRITIC SUPERALLOYS

Grant Number: DE-FE0005868
Performance Period: 10/01/2010-09/30/2013

Peter K. Liaw¹, Mark D. Asta², David C. Dunand³, Morris E. Fine³, Gautam Ghosh³, and C.T. Liu⁴
Ph.D. Students: Hong Ding², Shenyan Huang¹, Michael Rawlings³, Zhiqian Sun¹, Gian Song¹ and Zhenke Teng¹
Research Associate: Dr. Gongyao Wang¹ and Christian Liebscher²

1. Department of Materials Science and Engineering, The University of Tennessee (UTK), Knoxville, TN.
2. Department of Materials Science and Engineering, University of California, Berkeley (UCB), CA.
3. Department of Materials Science and Engineering, Northwestern University (NU), Evanston, IL.
4. Department of Mechanical Engineering, The Hong Kong Polytechnic University, Hung Hom, Kowloon, Hong Kong.

ABSTRACT

Ferritic superalloys strengthened by NiAl-type precipitates have received extensive attention as potential materials for high temperature applications. In this study, the B2-NiAl type precipitates and body-centered-cubic (BCC) Fe matrix in the Fe-Al-Ni-Cr-Mo system were thermodynamically described based on the alloy composition and aging temperature. Synchrotron X-ray diffraction and atom probe tomography were utilized to validate the calculated phase structure, composition, and volume fraction.

The impurity diffusivities of 5d transition-metal solutes in α -Fe have been calculated based on the harmonic transition-state theory, density-functional-theory calculations, semi-empirical corrections for magnetic contributions, and the Le Claire nine-frequency model. The calculation on the diffusion constants reveals that the atomic number demonstrates minimum values of D corresponding to Re and Os, at the center of the transition-metal series. The results for the impurity diffusivities are associated with minima and maxima in the computed solute-vacancy binding energy and migration energy, respectively.

1. INTRODUCTION

NiAl-type precipitate-strengthened ferritic steels have been highlighted as promising materials for the steam turbine applications¹⁻⁵. The lattice parameters of the body-centered-cubic (BCC) α -Fe and B2-ordered NiAl phase are more or less identical⁶. By adjusting the alloy composition, B2-NiAl precipitates can achieve a coherent-coplanar orientation to the BCC Fe matrix, which gives a feasibility of obtaining Fe-based superalloys with good creep resistance. It has been reported that recently developed Fe-Al-Ni-Cr-Mo alloys have excellent creep resistance, and their Larson–Miller parameters are higher than most of ferrite-based materials¹. Furthermore, it was found that the creep and ductility properties strongly depend on the elemental partitioning and precipitate volume fraction, which strongly depends on the overall alloy composition². In order to facilitate the design of an alloy, which meets the property requirements, it is urgent to establish a theoretical model to design those microstructures according to alloy compositions at the aging temperature. In the present study, the B2-NiAl type precipitates and BCC Fe matrix phase were thermodynamically calculated in the Fe-Al-Ni-Cr-Mo system. Synchrotron X-ray diffraction and atom probe tomography were then conducted to validate the calculated results.

Computational models and associated databases for diffusion constants in multicomponent alloys have been extensively studied since the relevance of diffusion for diverse phenomena occurs in materials processing^{7,8}. In this context, the impurity diffusion constants (D) are considered as a key factor, since they control the solute mobility depending on composition. In the absence of the experimental data, computational approaches to predict D are considerably significant. First-principles calculations based on the electronic density-functional theory (DFT) have been employed considerably. For example, calculations of D of substitutional impurities studied in this work have been carried out for Fe^{9,10}, Ni^{11,12}, and Al¹³ alloys. From such studies, a fundamental understanding of the mechanisms regarding variations in D with chemistry can be obtained. For example, it has long been accepted that the lowest values of D correspond to solutes greater than the matrix; first-principles calculations¹¹ have shown that this “rule-of-thumb” is not the general case, and revealed the importance of electronic-structure effects, which emphasize the application for DFT-based methods in computations of D.

Recently, we have reported computational calculations for impurity-diffusion coefficients in α -Fe based on Le

Claire's nine-frequency model¹⁴, utilizing a semi-empirical treatment of the effects of magnetic disorder, and density-functional-theory calculations of the relevant hopping frequencies for the zero-temperature ferromagnetic state¹⁵. In the present study, this approach is utilized to study 5d transition-metal solutes, Ta-Au, in BCC α -Fe. These elements are chosen due to the absence of experimental data, such that the present results are expected to be useful for the development of kinetic databases of ferritic alloys. Moreover, the present study is motivated to find slow diffusers of the 5d solutes in α -Fe, such that they may be effective in designing precipitation-strengthened alloys with reduced coarsening rates. In the remainder, we briefly review the computational formalism, and the computational results and compared with previous calculations and experimental results.

2. COMPUTATIONAL MODELING AND EXPERIMENTAL INVESTIGATIONS

2.1 THERMODYNAMIC MODELING

Thermodynamic calculations employed in the present study are established on the CALculation of PHase Diagram (CALPHAD) method¹⁶. The database of the Fe-Ni-Al-Cr-Mo system was established based on the PanFe and PanNi databases^{17, 18}. The substitutional solution model is utilized to describe both BCC and face-centered-cubic (FCC) phases: (Al, Cr, Fe, Mo, and Ni). The Gibbs energy is defined as:

$$G_m^\phi = \sum_i x_i G_i^{\phi,0} + RT \sum_i x_i \ln x_i + G^{ex,\phi} \quad (1)$$

The first term on the right hand of the equation represents x_i , the mole fraction of component, i , and $G_i^{\phi,0}$, the Gibbs energy of a pure component, i , with the ϕ structure, and ϕ is either the BCC or FCC structure; the second term is the ideal mixing term with R (gas constant), and T (temperature); the last term is the excess Gibbs energy of mixing, which is defined as:

$$G_m^{ex,\phi} = \sum_{i \neq j} x_i x_j \sum_v L_v^{i-j} (x_i - x_j)^v + \sum_{i \neq j \neq k} x_i x_j x_k \sum_{l=ijk} L_l^{i-j-k} V_l^{i-j-k} \quad (2)$$

The first term expresses the total binary interactions, and the second term indicates the total ternary interactions. L_v^{i-j} indicates binary interaction parameters for the i - j binary system, and L_l^{i-j-k} ternary interaction parameters for the i - j - k ternary system. V_l^{i-j-k} is expressed as:

$$V_l^{i-j-k} = x_l + \frac{1 - \sum_{q=ijk} x_q}{3} \quad (3)$$

Since contributions of the higher order interactions are minor, they are generally not necessary. The compound energy formalism was employed to express the B2 phase: (Al, Cr, Fe, Mo, and Ni)_{0.5}: (Al, Cr, Fe, Mo, Ni, and Va)_{0.5}. The Gibbs energy is defined as:

$$G_m^{B2} = \sum_i \sum_j y_i^I y_j^{II} G_{i;j}^{B2} + RT \left(0.5 \sum_i y_i^I \ln y_i^I + 0.5 \sum_i y_i^{II} \ln y_i^{II} \right) + G_m^{ex,B2} \quad (4)$$

y_i^I and y_i^{II} are the species concentrations of component, i , in the first and second sublattices, respectively. The first term on the right hand of the equation indicates the reference state with a mechanical mixture of the stable or hypothetical compounds: $i_{0.5}j_{0.5}$. $G_{i;j}^{B2}$ is the Gibbs energy of the stoichiometric compound, $i_{0.5}j_{0.5}$, with a B2 structure. The value of $G_{i;j}^{B2}$ can be attained experimentally, if $i_{0.5}j_{0.5}$ is a stable compound, or it can be a model parameter achieved by optimization using the experimental data relevant to the B2 phase. The calculated values are in good agreement with the experimental data. The second term is the ideal mixing Gibbs energy, which corresponds to the random mixing of species on the first and second sublattices, respectively. The last term is the excess Gibbs energy of mixing, which can be defined as:

$$G_m^{ex,B2} = \sum_{i,j,k} y_i^I y_j^I y_k^{II} \sum_v (y_i^I - y_j^I)^v L_{i,j;k}^v + \sum_{i,j,k} y_i^{II} y_j^{II} y_k^I \sum_v (y_i^{II} - y_j^{II})^v L_{k;i,j}^v + \sum_{i,j} y_i^I y_j^I y_i^{II} y_j^{II} L_{i,j;i,j} \quad (5)$$

The excess Gibbs energy indicates the interaction contributions from all the constituent binaries and ternaries. The "L" parameters in these terms are model parameters whose values are optimized, based on the experimental phase equilibrium and thermodynamic property data. These parameters can depend upon temperature. In this equation, a comma is used to separate species in the same sublattice, whereas a colon is used to separate species belonging to different sublattices.

2.2 EXPERIMENTAL

The alloy ingots were prepared by vacuum arc-melter using high purity metals (99.97% in purity), and then drop-cast into a Cu mold with the dimensions of 12.7 mm×12.7 mm×76.2 mm. The alloy FBB-8 (Fe-12.7Al-10.2Cr-9Ni-

1.9Mo, note that all the compositions are in atomic percent throughout this paper, unless specified otherwise) is the base alloy composition. By controlling amounts of Al, Ni, and Fe, FBB-13 (Fe-6.1Al-10.5Cr-9.3Ni-1.9Mo), FBB-12 (Fe-8Al-10.4Cr-9.2Ni-1.9Mo), and FBB-18 (Fe-18.9Al-9.8Cr-13Ni-1.8Mo) with different volume fractions of B2 precipitates can be achieved. The ingots were subsequently cut into 20 mm long rods. The rods were solution-treated at 1,200 °C for 30 min in evacuated and sealed quartz tubes, followed by air cooling, and then aged at 700 °C for 100 h. The average grain size of the alloy is ~100 μm and the average precipitate size is ~130 nm. The local electrode atom probe (LEAP[®]) analysis was conducted with a LEAP 4000X HR with a pulse repetition rate of 200 kHz and a voltage pulse fraction of 0.2, and at a specimen temperature of 60 K (−213 °C). The deviations of the atom probe tomography (APT) results were obtained from measuring at least two regions of the sample. The synchrotron high-energy X-ray diffraction on the specimens with a size of 12.7×12.7×1 mm³ were carried out with a high-energy X-ray (115 keV), and the diffraction patterns were recorded by a MAR-345 two-dimensional detector at the Advanced Photon Source, Argonne National Laboratory.

2.3 COMPUTATIONAL MODELING FOR IMPURITY DIFFUSIVITIES

The temperature dependence of D is defined as:

$$D = D_0 \exp(-Q/k_B T) \quad (6)$$

where D_0 is the pre-exponential factor, and Q is the activation energy. Considering a mono-vacancy mechanism, the exponential factor can be defined with the correlation factor (f_2), the lattice constant (a), the entropy of vacancy formation in BCC Fe (ΔS_v^f), the attempt frequency for the hopping of a solute atom to a nearest-neighbor vacancy (v^*), and the entropy of vacancy binding to a nearest-neighbor solute (ΔS_b), as follows:

$$D_0 = a^2 f_2 v^* \exp[(\Delta S_v^f + \Delta S_b)/k_B] \quad (7)$$

In Eq. 7, v^* can be expressed based on the harmonic transition-state theory¹⁹ as the quotient of the product of the vibrational frequencies corresponding to a configuration with a nearest-neighbor solute-vacancy pair ($v_i^{vac,sol}$) and the product of frequencies for a saddle-point configuration for the exchange of a solute and vacancy (v_i^{sad}): $v^* = \Pi v_i^{vac,sol} / \Pi v_i^{sad}$, where the product in the denominator excludes the imaginary frequency corresponding to motion along the diffusion path. In the case of impurity diffusion, the activation energy is the total vacancy formation energy in pure α -Fe (ΔH_v^f), and the migration energy for the solute-vacancy exchange (ΔH_m), the nearest-neighbor binding energy between a solute and vacancy (ΔH_v):

$$Q = \Delta H_v^f + \Delta H_v + \Delta H_m \quad (8)$$

In Eq. 7, the correlation factor (f_2) is defined in the model of Le Claire based on nine distinct jump frequencies, involving hops of the vacancy between sites within the second neighbor of the solute, as well as that in the BCC lattice far from the solute. Formulas for f_2 can be found in ref. 14. In general, f_2 can show an appreciable temperature dependence such that D_0 as defined above cannot be taken as independent of T .

As discussed previously²⁰⁻²², for α -Fe, the gradient of the self-diffusion versus impurity diffusion coefficients on an Arrhenius plot typically displays a distinct curvature below the Curie temperature. The dependence of Q on the state of magnetic order in the matrix contributes to this trend. Based on Girifalco²³, we describe the dependence of Q on magnetic disorder through the formula $Q^F(T) = Q^P [1 + \alpha S(T)^2]$, where α is dependent upon the kind of solute atoms, $S(T) = M(T) = M(T = 0 K)$ is the ratio of the magnetization at the temperature, T , to that at zero temperature, and $Q^F(T)$ and Q^P represent values in the ferromagnetic and paramagnetic states, respectively. The value of α for several solutes has been shown from plots of the experimental data over temperature ranges spanning the paramagnetic and ferromagnetic states²⁴. These results proposed²⁴ a linear relationship between the values of α and ΔM_{12} , the sum of the change in the local magnetic moments induced on the Fe atoms in the first and second neighbor shells of an impurity atom:

$$\Delta M_{12} = \sum_{i=1}^8 \Delta M_i^{1st} + \sum_{i=1}^6 \Delta M_i^{2nd} \quad (9)$$

In the current work, we utilize this empirical relation with the calculated magnitude of ΔM_{12} .

To calculate the properties, $Q^F(T = 0 K)$, and ΔM_{12} , and the parameters in Eq. 7, we have utilized spin-polarized DFT calculations within the generalized gradient approximation of Perdew, Burke and Ernzerhof (PBE)²⁵. The calculations utilized the projector augmented wave (PAW) method^{26, 27}, as implemented in the Vienna Ab Initio Simulation Package (VASP)²⁸⁻³¹, with a plane-wave cutoff of 300 eV. Monkhorst-Pack sampling³² of reciprocal space, with k-point grids equivalent to 12×12×12 for a conventional BCC unit cell was utilized. In order to characterize saddle-point geometries, diffusion paths were identified in a 4×4×4 bcc supercell using the climbing image nudged elastic band method³³, with a final optimization of the saddle-point configuration performed utilizing a force-based structural relaxation. For calculations of vibrational frequencies, we computed all of the $q = 0$ normal-

mode frequencies in a $3 \times 3 \times 3$ supercell using the frozen-phonon algorithm available in the VASP code.

3. RESULTS AND DISCUSSIONS

3.1 THERMODYNAMIC MODELING AND EXPERIMENTAL VALIDATION

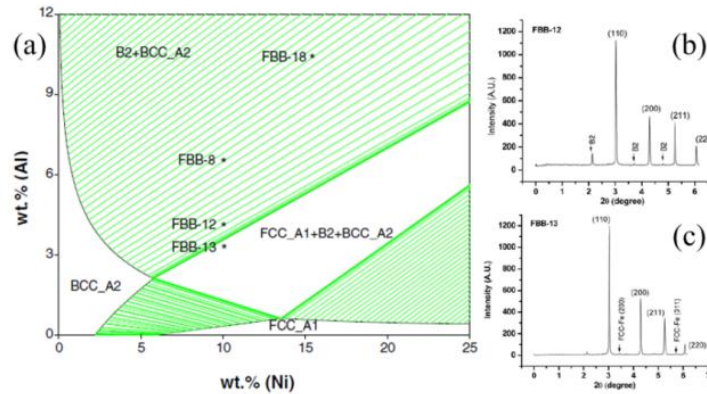


Figure 1. (a) Calculated isothermal section of Fe-Al-Ni-10Cr-2Mo (weight percent) system at 700 °C, and synchrotron high-energy X-ray diffraction of alloys (b) FBB-12 and (c) FBB-13.

The isothermal section of Fe-Ni-Al-10Cr-2Mo (wt.%) at 700 °C is computed, since the aging temperature of the studied alloys is 700 °C. Figure 1(a) shows the compositions of the four model alloys. To describe an isothermal section of a five-component system, two elements are necessary to have fixed compositions. All the other 4 alloys, except for the alloy FBB-13, locate in the BCC+B2 two-phase field, as shown in Fig. 1(a), which is in good agreement with a previous TEM study¹. It is interesting that the composition of FBB-13 is located in the BCC+B2+FCC three phase field along the BCC+B2/BCC+B2+FCC phase boundary, whereas FBB-12 is placed in the BCC+B2 two-phase field. Synchrotron high-energy X-ray diffraction was utilized for these two alloys to validate the phases formed in FBB-12 and FBB-13. Figs. 1(b) and (c) show the diffraction patterns revealing that FBB-12 consists of BCC and B2, whereas FBB-13 contains a small amount of the FCC Fe. It is believed that the formation of the FCC phase stems from the low Al/Ni ratio in FBB-13, since Al is a ferrite (BCC) forming element in Fe, whereas Ni is an austenite (FCC) forming element.

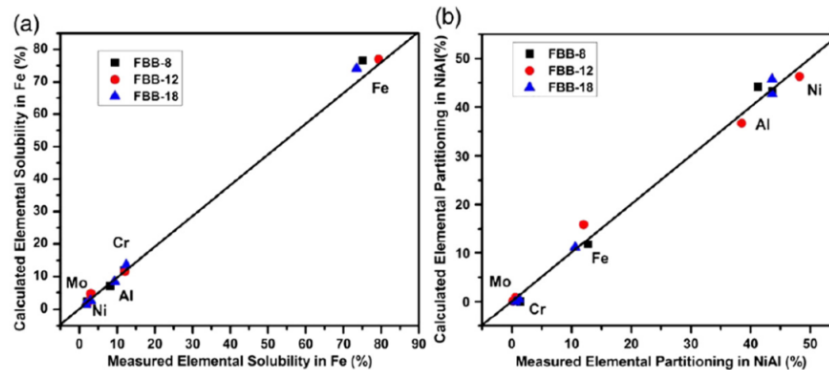


Figure 2. Comparisons between the calculated and experimental results showing: (a) elemental solubilities in the Fe matrix, and (b) elemental partitioning in NiAl. Note that the data points of some elements in (a) and (b) overlap with each other as their concentrations are very similar.

Figure 2 displays comparisons between calculated and experimentally determined phase compositions for the matrix and the precipitate phases of the alloys. It is observed that all the data points are in good accordance between the calculated and experimental results. Moreover, the compositions of the Fe matrix and NiAl precipitates were determined by counting the collected ions from APT. Assuming that only the BCC Fe matrix and B2 precipitate are present in the microstructure, the B2-precipitate volume fraction was measured based on the lever rule. If a third phase or a significant solute segregation form in the microstructure, such as dislocations or grain boundaries, the estimated B2 precipitate volume fraction will be revised.

From the thermodynamic calculations and APT results, the precipitates are of NiAl-type with some Fe partitioning inside. Figures 3 (a)-(e) displays representative atom maps of different elements in FBB-12. Cr preferentially remains in the Fe-matrix (Fig. 3d), suggesting that the NiAl-type precipitates do not contain Cr. This feature is effective in the alloy design, because the addition of Cr leads to the increased oxidation resistance of the Fe matrix. It is observed that a significant amount of Al remain in the Fe matrix, as shown in Fig. 3, which could induce a low ductility of the studied alloys³⁴. The concentration of Al in the matrix needs to be optimized. In the previous study¹, α -Fe particles inside some of the B2-ordered precipitates were observed. This trend implies that the measured Mo content in the α -Fe particles contributes to that of the B2 phase. Since the Fe matrix consists of a higher amount of Mo than that of the B2-ordered precipitates, the measured Mo composition is therefore higher than the actual Mo composition in B2. This point is further supported by alloy FBB-12, in which no α particles were found in B2 as shown by the atom maps in Fig. 3. The measured Mo content in B2 for this alloy is 0.2 at.%, which agrees with the calculated value (0.1 at.%) well. On the other hand, there is a relatively large discrepancy between the calculation and experimental measurement of Mo concentrations in the B2-ordered precipitates. In FBB-8, negligible solubility of Mo in the B2 precipitate is calculated, whereas the experimental measurement shows 1.4 at.%. This deviation can be explained from both calculation and experimental point of views. Since B2 is not stable in the Mo-X (X represents Fe, Al, Ni or Cr) binary systems, this thermodynamic description of the B2 phase in these binaries is not as accurate as it is in other binaries, such as Fe-Al and Ni-Al systems.

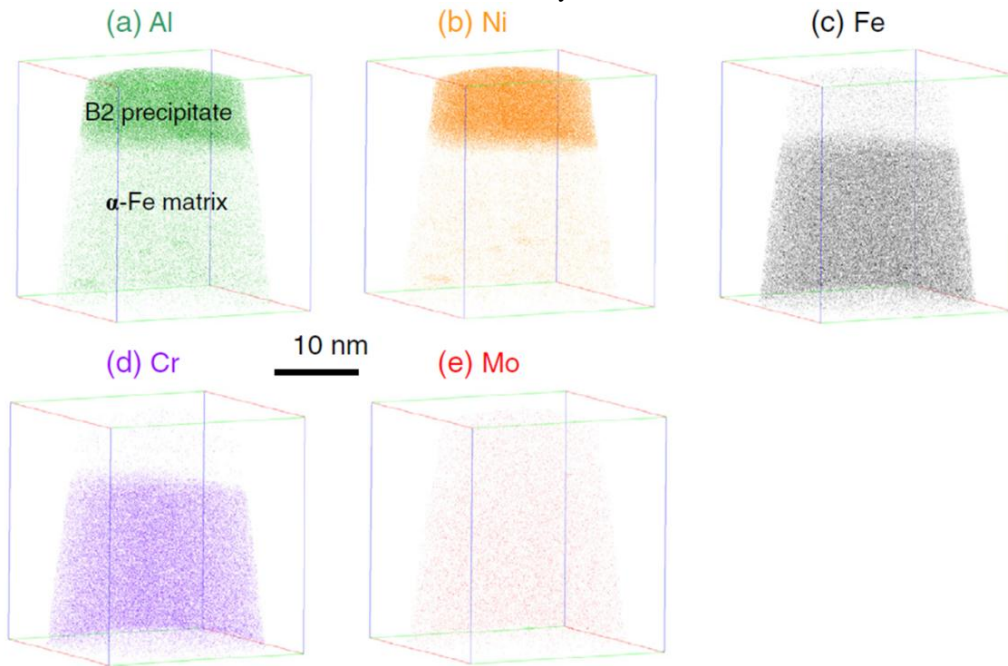


Figure 3. Representative atom maps of different elements in the alloy FBB-12.

3.2 IMPURITY DIFFUSIVITIES FOR 5D TRANSITION METAL SOLUTES IN α -FE

Figure 4 shows ΔH_b and ΔH_m as a function of the atomic number of the 5d solute species. It is well acceptable that negative values of ΔH_b imply an attractive interaction between the vacancy and solute, and the more negative the magnitude the larger the effect on reducing the quantity of Q . Figure 4 (a) exhibits that the strongest binding is achieved for solutes at the beginning and end of the transition-metal series, whereas Re and Os located in the middle of the transition-metal series display the weakest binding. This trend agrees with recent calculations attained for ΔH_b as a function of atomic numbers for 4d solute elements in α -Fe¹⁵. Figure 4 (a) exhibits the atomic radius across the series. By comparing these values with ΔH_b , it is observed that the largest solute atoms cause largest magnitudes for the binding energies. This trend was observed in transition-metal solute elements in Ni¹¹, and the results support that large solute atoms tend to be near vacancies to reduce elastic energy. However, the correlation between the size and ΔH_b in Fig. 4 (a) is not perfectly reliable, since Ta is estimated to possess the largest binding energy in spite of the fact that its atomic radius is slightly smaller than that of Au, and both Os and Re are expected to show very similar magnitude of ΔH_b in spite of the smaller size of the former.

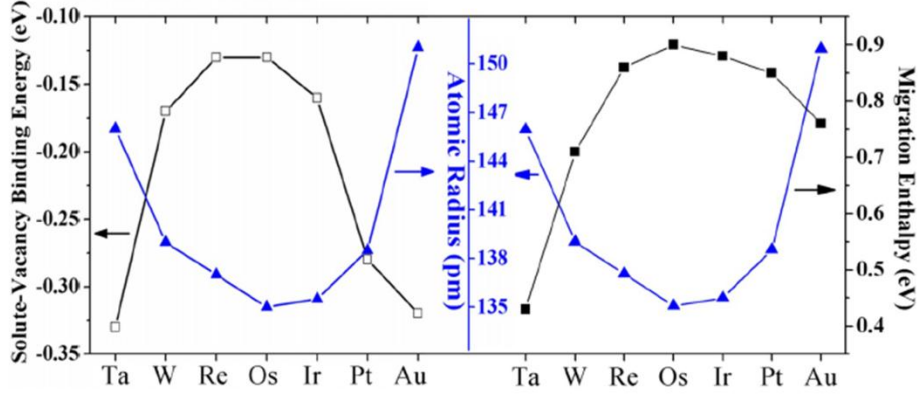


Figure 4. Dependence of the solute-vacancy binding and migration energies on atomic radius (i.e., Goldschmidt radii) for 5d transition element series

Similarly, the migration energy exhibits a clear tendency according to the atomic number of the solute species. Particularly, Os possesses the maximum value of ΔH_m , which is located in the middle of the transition-metal series, and as the values decrease with increasing or decreasing the atomic number. The trend seems unreasonable, since the solute species with the smallest atomic radius is favorable to the largest values of ΔH_m . Nonetheless, previous calculations show a similar trend towards larger values of ΔH_m for smaller solute atoms, e.g., for Ni-based alloys¹¹.

Energy/Factor	Element	Ta	W	Re	Os	Ir	Pt	Au
ΔH_b		-0.33	-0.17	-0.13	-0.13	-0.16	-0.28	-0.32
ΔH_m		0.43	0.71	0.86	0.90	0.88	0.85	0.76
Q^F		2.30	2.74	2.93	2.97	2.92	2.77	2.64
α		0.06	0.09	0.08	0.12	0.18	0.24	0.25
Q^P		2.17	2.52	2.71	2.65	2.48	2.23	2.11
F_2		0.03	0.73	0.93	0.97	0.96	0.90	0.57
D_0		4.04	138	298	310	118	67	21

Table 1. Solute-vacancy binding enthalpy ΔH_b , solute migration enthalpy ΔH_m and the ferromagnetic Q^F in α -Fe all in units of eV, are in the first three rows, respectively. The Q^P is derived as $Q^P = Q^F = (1 + \alpha)$. The correlation factors, f_2 , and diffusion pre-exponential factors, D_0 (mm²/s), obtained by the Le Claire's model, corresponding to 1,000 K, are listed in the last two rows.

Table 1 summarizes the calculated results for D_0 at the representative temperature of 1,000 K, showing strong differences between the solute species. While the values for W, Re, Os, Ir, and Pt are in reasonable accordance with values reported for self-diffusion in α -Fe and for impurity-diffusion coefficients available for 4d and 5d impurities (see ref. 9 and references therein), the values for Au and especially Ta are significantly low. The low value of D_0 for Ta results from the low value of the correlation factor ($f_2 = 0.03$), indicating the strong solute-vacancy binding for this species, which leads to a high fraction of solute-vacancy hops, followed by hops back to the original solute position. It has been reported that Y in Fe³⁵ possess low values of f_2 . The low value of D_0 for Au is attributed to a large negative value for the vacancy-solute binding entropy.

Figure 5 shows the results for the measured values of α against the calculated values of the quantity, ΔM_{12} , defined in Eq. 9. Assuming a linear relationship, the solid line indicates a least-squares fit of the data. The circle symbols represent the predicted values of α from this linear fit, using the corresponding calculated values of ΔM_{12} . A clear tendency in the results is observed that as the atomic number increases from Hf to Au, the calculated value of ΔM_{12} increases monotonically. The largest dependence of Q on magnetic order [i.e., $S(T)$] is thus predicted for Pt and Au.

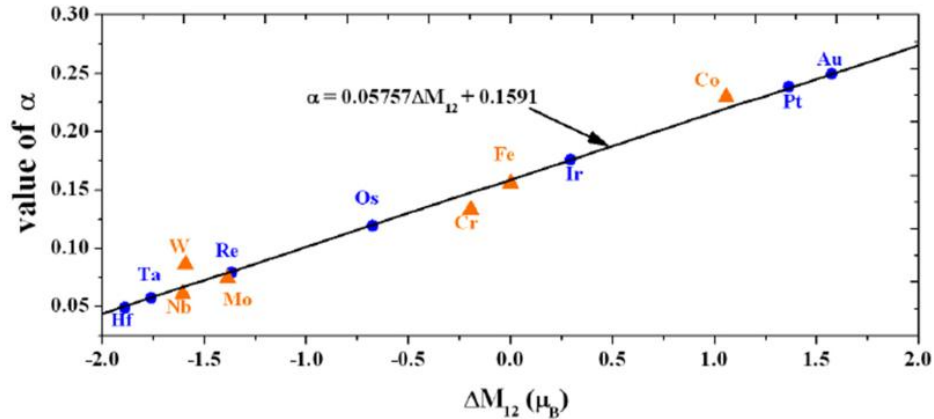


Figure 5. The linear relationship between α and ΔM_{12} . The triangles denote the parameter is derived from experiments and the circles are calculated from the linear relationship.

Figure 6 exhibits the temperature dependencies of the calculated impurity diffusion coefficients in α -Fe. Note that the results for the self-diffusion in α -Fe calculated in ref. 9 based on the same computational calculation are also included in Fig. 6. By comparing the results in the paramagnetic state (from 1,043 to 1,183 K), it is observed that the values of D can be separated into three groups. The first is the solutes with D values higher than that for self-diffusion in Fe (Pt and Au). The second group consists of solute atoms with D comparable to that for self-diffusion (W, Ir, and Ta: the similar D for Ta and W obtained here is contrary to the values for inter-diffusion measurements reported in ref. 36 for more concentrated alloys, where Ta shows much larger values). The third group is the “slow diffusers” with values of D lower than that for self-diffusion (Re and Os). The relatively low values of D for these solute species are linked to the larger values of ΔH_m and smaller magnitudes for ΔH_b . Re has the lowest calculated impurity diffusion coefficient among all the solute species in this work, with a value of D that is an order of magnitude lower than that for self-diffusion at temperatures near 1,000 K. It is believed that these solute species are considered as potential additions to precipitation-strengthened ferritic alloys to reduce coarsening rates at high temperatures.

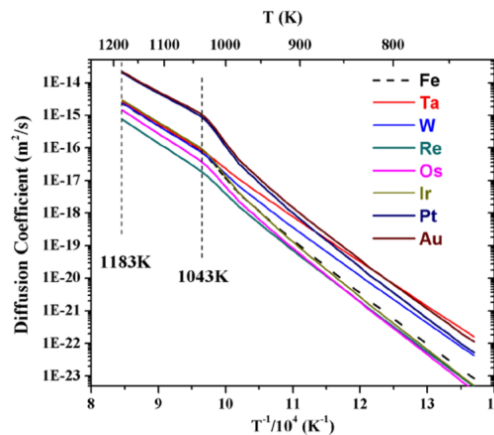


Figure 6. Calculated temperature dependence of diffusion coefficients for 5d transition metal solutes in α -Fe. The dashed line corresponds to our previous calculation of the self-diffusion coefficient in α -Fe.

4. CONCLUSION

The volume fraction, composition, and structure of the BCC Fe matrix and B2-NiAl precipitates in the Fe-Al-Ni-Cr-Mo system were calculated based on the thermodynamic modeling in terms of the composition at the aging temperature. The thermodynamic calculation exhibited that a low Al/Ni ratio induces formation of FCC phase, as confirmed by synchrotron X-ray diffraction. Atom probe tomography was carried out to determine the phase compositions and volume fractions. Thermodynamic calculations is in good agreement with the experimental results. We calculated impurity diffusion coefficients based on first-principles, and correlated migration energies,

correlation factors, and solute-vacancy binding energies for 5d transition metal solutes in α -Fe. The migration energies and solute-vacancy binding enthalpy are linked to the atomic number, showing maximum values for Re and Os in the middle of the transition-metal species. This trend is reflected in the calculated result that Re and Os possess the slowest impurity diffusion coefficients.

ACKNOWLEDGEMENTS

We are very grateful to (1) Richard Dunst, (2) Veto Cedro, (3) Nicholas Anderson, and (4) Patricia Rawls for their kind support and encouragement, and (5) the National Energy Technology Laboratory (NETL) for sponsoring this project.

REFERENCES

- [1] Teng ZK, Miller MK, Ghosh G, Liu CT, Huang S, Russell KF, Fine ME and Liaw PK, *Scr. Mater* 63 (2010) 61
- [2] Teng ZK, Liu CT, Ghosh G, Fine ME, Liaw PK, *Intermetallics* 18 (2010) 1437
- [3] Huang S, Worthington DL, Asta M, Ozolins V, Ghosh G, Liaw PK, *Acta Mater.* 58 (2010) 1982
- [4] Zhu SM, Tjong SC, Lai JKL, *Acta Mater.* 46 (1998) 2969
- [5] Stallybrass C, Sauthoff G, *Intermetallics* 13(2005) 1263
- [6] Villars P, Calvert LD, *Pearson's handbook of crystallographics data for intermetallic phases.* Metal Park, OH: ASM; 1985
- [7] Andersson JO, Helander T, Hglund L, Shi P, Sundman B, *Calphad* 26 (2002) 273
- [8] Anton Ven der V, Hui-Chia Y, Gerbrand C, Katsuyo T, *Progr. Mater. Sci.* 55 (2010) 61
- [9] Huang S, Worthington DL, Asta M, Ozolins V, Ghosh G, Liaw PK, *Acta Mater.* 58 (2010) 1982
- [10] Choudhury S, Barnard L, Tucker J, Allen T, Wirth B, Asta M, Morgan D, *J. Nuclear Mater.* 411 (2011) 1
- [11] Janotti A, Krcmar M, Fu CL, Reed RC, *Phys. Rev. Lett.* 92 (2004) 085901
- [12] Krcmar M, Fu C, Janotti A, Reed R, *Acta Mater.* 53 (2005) 2369
- [13] Sandberg N, Holmestad R, *Phys. Rev. B* 73 (2006) 014108
- [14] Le Claire AD, *Philos. Mag.* 21 (1970) 819
- [15] Gorbатов OI, Korzhavyi PA, Ruban AV, Johansson B, Gornostyrev YN, *J. Nuclear Mater.* 419 (2011) 248
- [16] Zhang F. *Advances in Materials Technology for Fossil Power Plants, Proceedings from the Fourth International Conference.* Hilton Head Island, SC: ASM; 2004
- [17] *PanFe-Thermodynamic Database for Multicomponent Iron Alloys.* Madison, WI 53719: CompuTherm, LLC; 2000
- [18] *PanNi-Thermodynamic Database for Multicomponent Nickel Alloys.* Madison, WI 53719: CompuTherm, LLC; 2000
- [19] Vineyard GH, *J. Phys. Chem. Solids* 3 (1957) 121
- [20] Hettich G, Mehrer H, Maier K, *Scripta Metal.* 11 (1977) 795
- [21] Oono N, Nitta H, Iijima Y, *Mater. Trans.* 44 (2003) 2078
- [22] Nitta H, Iijima Y, *Phil. Mag. Lett.* 85 (2005) 543
- [23] Girifalco L, *J. Phys. Chem. Solids* 23 (1962) 1171
- [24] Iijima Y, *J. Phase Equilib. Diff.* 26 (2005) 466
- [25] Perdew JP, Burke K, Ernzerhof M, *Phys. Rev. Lett.* 77 (1996) 3865
- [26] Blochl PE, *Phys. Rev. B* 50 (1994) 17953
- [27] Kresse G, Joubert D, *Phys. Rev. B* 59 (1999) 1758
- [28] Kresse G, Hafner J, *Phys. Rev. B* 47 (1993) 558
- [29] Kresse G, Hafner J, *Phys. Rev. B* 49 (1994) 14251
- [30] Kresse G, Furthmuller J, *Comp. Mater. Sci.* 6 (1996) 15
- [31] Kresse G, Furthmuller J, *Phys. Rev. B* 54 (1996) 11169
- [32] Monkhorst HJ, Pack JD, *Phys. Rev. B* 13 (1976) 5188
- [33] Henkelman G, Uberuaga BP, Jonsson H, *The J. Chem. Phys.* 113 (2000) 99
- [34] Herrmann J, Inden G, Sauthoff G. *Acta Mater.* 51 (2003) 2847
- [35] Murali D, Panigrahi B, Valsakumar M, Sundar C, *J. Nuclear Mater.* 419 (2011) 208
- [36] Shaikh QA, *Mater. Sci. Tech.* 6 (1990) 1177